Coupled Climate Responses to Recent Australian Wildfire and COVID-19 Emissions Anomalies Estimated in CESM2

J. T. Fasullo[*,†], N. Rosenbloom, R. R. Buchholz, G. Danabasoglu, D. M. Lawrence, and J.-F. Lamarque

[1]National Center for Atmospheric Research, Boulder, CO, USA.

Corresponding author: John Fasullo (fasullo@ucar.edu)

Key Points:

- The response to COVID-19 in CESM2 is modest, amounting globally to a peak 0.23±0.14 W m^{-2} heating and 0.05±0.04 K warming through 2022
- In contrast, the Australian wildfires cool the globe by 0.95±0.15 W m^{-2} in Dec 2019 and 0.06±0.04 K by mid-2020
- Significant water cycle responses are driven by Australian wildfires, including a northward displacement of tropical deep convection

Abstract

Multiple 50-member ensemble simulations with the Community Earth System Model version 2 are performed to estimate the coupled climate responses to the 2019-2020 Australian wildfires and COVID-19 pandemic policies. The climate response to the pandemic is found to be weak generally, with net top-of-atmosphere radiative anomalies of +0.23±0.14 W m^{-2} driving a gradual global warming of 0.05±0.04 K by the end of 2022. While regional anomalies are detectible in aerosol burdens and clear-sky radiation, few significant anomalies exist in other fields due to internal variability. In contrast, the simulated response to Australian wildfires is a strong and rapid cooling, peaking at −0.95±0.15 W m^{-2} in late 2019 with an anomalous global cooling of 0.06±0.04 K by mid-2020. Transport of fire aerosols throughout the Southern Hemisphere increases albedo and drives a strong interhemispheric radiative contrast, with simulated responses that are consistent generally with those to a Southern Hemisphere volcanic eruption.

Plain Language Summary

Significant perturbations in aerosol and other climate forcing emissions accompanied both the 2019-2020 Australian wildfires and the COVID-19 pandemic-induced changes in human activity. This analysis estimates the coupled climate response to each event in 50-member simulation ensembles using the Community Earth System Model version 2. The simulations depict a modest climate warming that evolves gradually through 2022 driven by COVID-19 pandemic responses with a timing and initial magnitude consistent with recent meteorological studies. In contrast, a strong and abrupt climate cooling resulting from Australian wildfire emissions is simulated, with global-scale responses arising in part from contrasts in radiation anomalies between hemispheres. Responses to wildfires include a northward displacement of tropical deep convection, similar to what is seen after major extratropical volcanic eruptions, suggesting the potential for an influence on the El Niño / Southern Oscillation.

1 Introduction

Multiple episodes of anomalous climate forcing have occurred in recent years. These include the biomass burning emissions anomalies from the 2019-2020 Australian wildfire season (hereafter referred to as AF), and anthropogenic emissions perturbations arising from the response to the spread of the Coronavirus Disease 2019, which began in Jan 2020 and continues through the present (hereafter referred to as COVID). While significant effort has been spent on diagnosing the climate effects of these events, understanding the coupled response to each and estimating the broader significance of the responses remains a work in progress.

The 2019-2020 AF season was singular in its severity and associated particulate emissions (Khaykin et al., 2020; Hirsch and Koren, 2021). While Australia is known as a landscape that experiences frequent bushfires, extreme bushfires with associated pyrocumulonimbus have been increasing over the last few decades and are predicted to increase even further in coming decades (Sharples et al., 2016; Dowdy et al., 2019). The extreme AF season in 2019-2020 had devastating consequences for lives, ecosystems, and property, including wide-scale smoke impacts across the southeast of the continent (Wintle et al., 2020). Additionally, hemispheric transport of fire pollution at low and lofted altitudes created atmospheric signatures over New Zealand and South America. This pollution remained in the atmosphere for well over three months, with solar heating of a stable, dense smoke plume creating a localized stratospheric ozone-hole and circulation response (Khaykin et al., 2020). While the amount and persistence of associated aerosol burdens have drawn parallels to major volcanic eruptions, an understanding of similarities in the climate response will depend on a more complete analysis and modeling of the event.

The climate response to COVID has received broad attention and recent modeling studies have quantified the local radiative response to the emissions reductions associated with an unprecedented disruption of manufacturing and transportation sectors. Both Ming et al. (2020) and Gettelman et al. (2020) adopted “nudged” meteorology experiments to estimate the regional radiative anomalies associated with these disruptions. These analyses identify large reductions in regional clear-sky albedo (~7%) and aerosol optical depth (32%, Ming et al., 2020), with an associated global increase in effective radiative forcing of 0.29±0.15 W m^{-2} (Gettelman et al., 2020). Even on regional scales, however, disentangling the radiative effects of COVID from internal variability is a challenge as only about a third of east Asia’s anomalous clear-sky shortwave flux can be attributed to COVID at its peak in March 2020 (Ming et al., 2020; Loeb et al., 2021). While nudged meteorology experiments are useful for isolating the initial effects of small signals such as COVID from internal variability, they do not address the broader coupled response of the climate system. Examples of such responses include changes in the ocean and associated feedbacks in the atmosphere and coupled internal modes. As prolonged emissions anomalies associated with COVID are anticipated (Forster et al., 2020), such nudged experiments do not provide a framework for estimating the climate response in coming years, either. Recent efforts to address the coupled response include Fyfe et al. (2021), where the responses to various idealized COVID emissions reductions are explored in an Earth System Model, and Jones et al. (2021), where a dozen such models are used to estimate both the climate response and its model dependence. These studies have generally found the climate response to be weak, with Fyfe et al. (2021) estimating a global near-surface warming of roughly 0.04K for a 25% emissions reduction by the end of 2022 and Jones et al. (2021) unable to detect any change in warming or precipitation.

In this work, we therefore seek to further explore these issues using the Community Earth System Model version 2 (CESM2; Danabasoglu et al., 2020). We use best-estimates of emissions from the Australian wildfires generated from satellite data and use the community-adopted COVID emissions scenario (Lamboll et al., 2020a) used in Jones et al. (2021) to generate simulation ensembles that extend from July 2019 through 2024 using a broad range of initialized states. As these ensembles are large (50 members), they allow for a more precise estimation of forced responses and associated uncertainties than in Jones et al. (2021) in one of the best performing climate models available (see Methods). Details of the forcing datasets, climate model, initialization, and analysis methods are given in section 2, and large-scale aspects of the climate responses are shown and discussed in section 3. A synthesis discussion of results, caveats, broader significance, and future work is provided in Concluding Remarks in section 4.

2 Materials and Methods

2.1 The Community Earth System Model

The CESM2 is the newest coupled Earth system model developed at the National Center for Atmospheric Research (NCAR) in partnership with universities and other research institutions (Danabasoglu et al., 2020). The model incorporates a range of new capabilities and improvements that are directly relevant to the simulation of climate responses to wildfire and COVID emissions anomalies. These include new chemical and physical representations of direct and indirect aerosol effects and their interactions with clouds. An improved treatment of aerosols is provided by the Modal Aerosol Model version 4 (Liu et al., 2016). The Morrison−Gettelman cloud microphysics scheme has also been updated (Gettelman & Morrison, 2015), and mixed phase ice nucleation is improved to depend on both aerosols and temperature, following Hoose et al. (2010), Wang et al. (2014), and Shi et al. (2015). A key additional advance is the implementation of a unified turbulence scheme that provides a uniform treatment of clouds across cloud types (Bogenschutz et al., 2013), replacing their more idealized and disjoint representations in earlier model versions. Many other advances are also included in CESM2, and a recent evaluation of available climate models identifies CESM2 as being among the most skillful of these models, based on metrics that compare the model outputs against present−day observations (Fasullo 2020).

2.2 Prescribed Forcings

Reductions in anthropogenic emissions due to COVID are from version 4 of the Lamboll et al. (2020b) dataset which combines national mobility data with analysis from Le Quéré et al. (2020) to estimate sector-based emissions (Forster et al., 2020). The emission scenario follows a “2-year-blip” trajectory, based on the assumption that 66% of the June 2020 reduction in emissions persists until the end of 2021, after which emissions linearly recover to the pre-COVID emission trajectory in the Shared Socioeconomic Pathway (SSP245) by the end of 2022 (Forster et al., 2020).

Fire emissions are prescribed use biomass burning estimates of trace gases and aerosols from the Global Fire Emissions Database version 4 with small fires (GFED4s), described in van der Werf et al. (2017). The emissions are created from satellite-measured burned area (Giglio et al., 2013) with small fires added using satellite-measured fire-count information (Randerson et al., 2012). Emissions are conservatively regridded to 0.9° (latitude) x1.25° (longitude) horizontal resolution for use in CESM2. Species with emissions incorporated include black carbon, primary organic matter (calculated as GFED4s organic carbon scaled by 1.4 to account for the other elements present in organic aerosols), dimethyl sulfide (DMS), and sulfur dioxide and sulfate aerosol (2.5% of GFED4s SO_2 is emitted directly as sulfate, with the remainder as SO_2). We do not perturb concentrations of ozone and other oxidants as this will have a limited climate impact. We do however include a lumped semivolatile organic gas-phase species that accounts for the creation of secondary organic aerosols (SOAG), by combining GFED4s species (higher alkanes, higher alkenes, toluene, benzene, xylenes, isoprene, and terpenes) that are then multiplied by a factor of 1.5 (Tilmes et al., 2019). Our fire emissions are aligned with the Coupled Model Intercomparison Project phase 6 (CMIP6), which uses GFED4s to anchor historical fire emissions (van Marle et al., 2017). After 2018, fire emissions for all ensembles are from SSP245 with the exception of our Australian fire ensemble, as described below.

Smoke interacts with radiation in multiple ways. There is large variability in the overall radiative impact due to variability in smoke loadings and properties such as particle composition and size. Smoke particles may be absorbing (mainly black carbon) or scattering (mainly organic matter, Sokolik et al., 2019). The observationally constrained cloud-free direct radiative forcing from the AF was estimated to be −3.0 W m^{-2} at the surface between 25°S and 60°S when averaged across all longitudes for February 2020 (Khaykin et al., 2020). Interaction of smoke with clouds further complicates radiative estimates. For example, smoke particles can serve as cloud condensation nuclei (Sokolik et al., 2019). Additionally, the interaction of aerosol heating with cloud formation also depends on whether the smoke is emitted within or above the planetary boundary layer, and whether the smoke is over land or ocean (Sokolik et al., 2019). Globally for black carbon, the interaction with clouds is estimated to almost completely counteract warming properties (Stjern et al., 2017). CESM2 provides the opportunity to simulate all of these processes and interactions, and estimate their climate effects.

2.3 Ensemble Experiments

The experiments conducted are summarized in Figure 1. A 10-member ensemble of simulations for the 2015-2024 period with the SSP2-4.5 forcing serves to estimate background conditions in the absence of interannual variability in biomass burning emissions. Aside from the gradual warming associated with increases in effective radiative forcing, no significant transient climate responses are identified in this ensemble (see discussion). An analogous 10-member set of simulations (GSSP245) is performed from 2015 through July 2019 using the GFED4s-based fire forcing estimates (described above) through 2018. Notably, the fire emissions in the GSSP245 scenario is more consistent with historical fire emissions used in previously run historical simulations that were used to provide 2015 initialized states in that, unlike in SSP245, observed interannual variability is prescribed in biomass burning emissions (van Marle et al., 2015). Both the SSP245 and GSSP245 ensembles are initialized on 01 January 2015 from CESM2 historical-era simulations that use standard CMIP6 historical forcings. These initial states are selected to provide a diversity of phases in major modes of internal variability such as the El Niño / Southern Oscillation (ENSO). Two sets of 50-member ensembles initialized from the 10 GSSP245 simulations using small (i.e. micro) atmospheric perturbations are then conducted for the 2019-2024 period with one set using the COVID emissions datasets and the other with both COVID and AF datasets. The respective ensembles are referred to as COVID and COVID+AF, the latter of which incorporates GFED4s-based fire emissions over Australia from July 2019 through June 2020 only and SSP245 prescriptions elsewhere and afterward. To provide a comparable ensemble size to gauge the COVID and AF responses, the number of members for GSSP245 is increased to 50 for the July 2019 – 2024 period. The July start date from these runs is motivated by the identical forcings used across all three ensembles before that date. The combined response to AF and COVID is computed by differencing the COVID+AF and GSSP245 ensemble means. Climate responses to AF only are estimated by differencing the COVID+AF and COVID ensemble means while responses to COVID are estimated from differencing the COVID and GSSP245 ensemble means.

To further reduce the influence of internal variations in our analysis, temporal smoothing is applied. Forcings associated with COVID emissions reductions are anticipated to persist through 2022 (Forster et al., 2020) whereas the majority of emissions anomalies from the AF occurred in Dec 2019 and Jan 2020, becoming small within months (Khaykin et al., 2020). Motivated by the contrasting timescales and magnitudes of the events, a seasonal (1-3-5-6-5-3-1) Gaussian smoother is applied to resolve wildfire climate responses while a 13-month averaging, where the end months are given weights of 0.5, is applied to resolve large-scale responses to COVID. In our analysis of spatial structures in Figures 2 and 4, the Gaussian smoother is used for all fields.

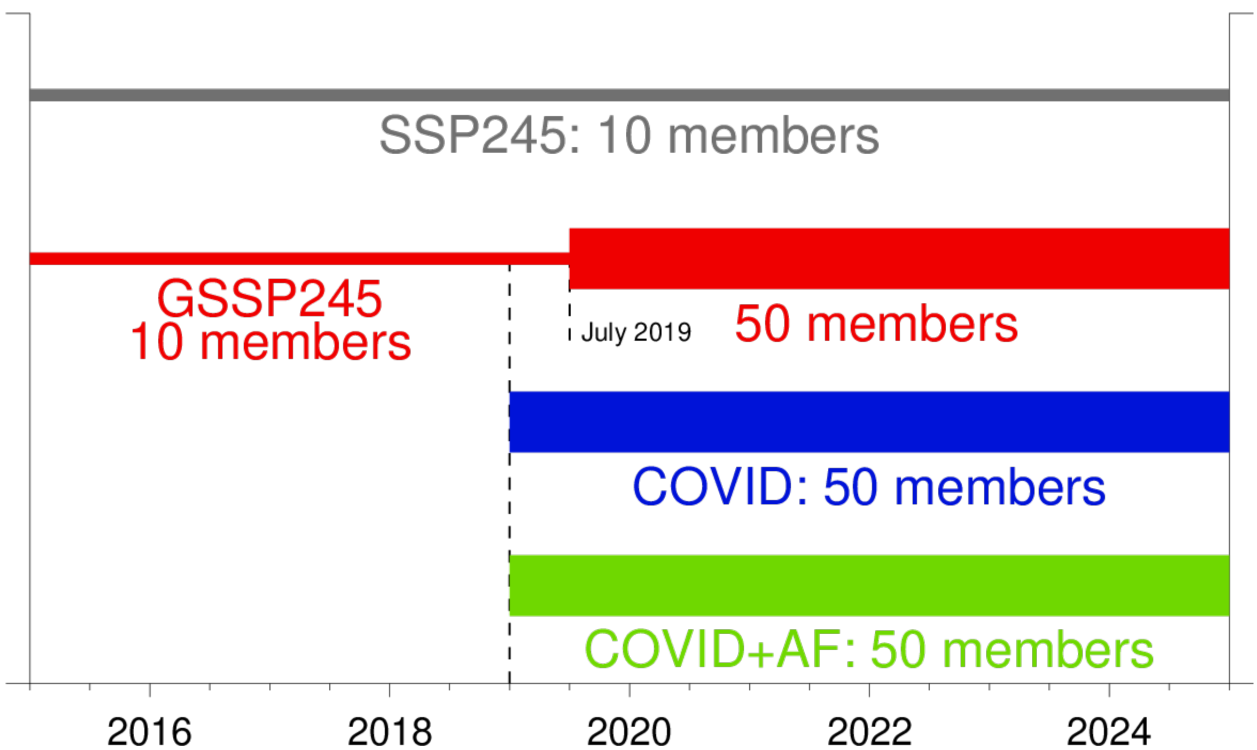

Figure 1: Description of CESM2 simulations used in this study, including the control background ensemble (SSP245, grey, 10 members), a 10-member spin-up ensemble that uses SSP245 and also incorporates estimated wildfire emissions from GFEDv4s from 2015 through 2018 (GSSP245, red), and a 50-member extension through 2024. Ensembles of members incorporating estimated COVID-19 (COVID, blue), and COVID-19 plus Australian wildfire emissions anomalies (COVID+AF, green) extend from January 2019 through 2024.

3 Spatiotemporal Structure of COVID and AF Climate Responses

The zonal-mean temporal evolution of key ensemble-mean aerosol burdens and top-of-atmosphere (TOA) radiative flux anomalies due to COVID+AF are shown in Figure 2. Both the AF and COVID driven emissions anomalies are generally distinct in black carbon (BC) and sulfate aerosol burdens (Figures 2a, 2b). Positive anomalies spanning the tropics and Southern Hemisphere (SH) from mid-2019 through mid-2020 in BC are consistent with the AF response (not shown). These anomalies are relatively short-lived and by March 2020 are largely indistinguishable from internal variability. Beginning in early 2020 negative anomalies consistent with the COVID response emerge from 10°-45°N in both BC (Figure 2a) and sulfate (Figure 2b), peaking in early 2020 and lasting through late 2022 – the recovery period of the "2-yr blip" scenario. The persistence of negative burden anomalies is generally coherent in time and space with the emissions anomalies themselves. Detectible anomalies in aerosol burdens span broad latitudinal ranges, particularly for sulfate burdens as the perturbations greatly exceed internal variability. In contrast, the radiative influence of aerosol burdens is in instances obscured by internal variability in both clear-sky and all-sky conditions, an effect remarked upon for COVID by Ming et al. (2020), Gettelman et al. (2020), and Loeb et al. (2021). However, a statistically detectable negative anomaly in ensemble-mean net downward clear-sky shortwave flux (SW_{CS}, Figure 2c) is coincident with anomalous AF BC burdens. While the SW_{CS} anomaly magnitude is modest (~0.4 W m^{-2}), the associated net TOA radiative flux (R_T) anomalies (Figure 2d) are strong (>2 W m^{-2}), extending across most of the SH. As discussed below, these anomalies likely arise from aerosol-cloud interactions. While radiative anomalies coincident with COVID burden anomalies are not detectible in the presence of internal variability, collocated anomalies are generally positive and therefore consistent with the anticipated radiative effects of reduced aerosol burdens.

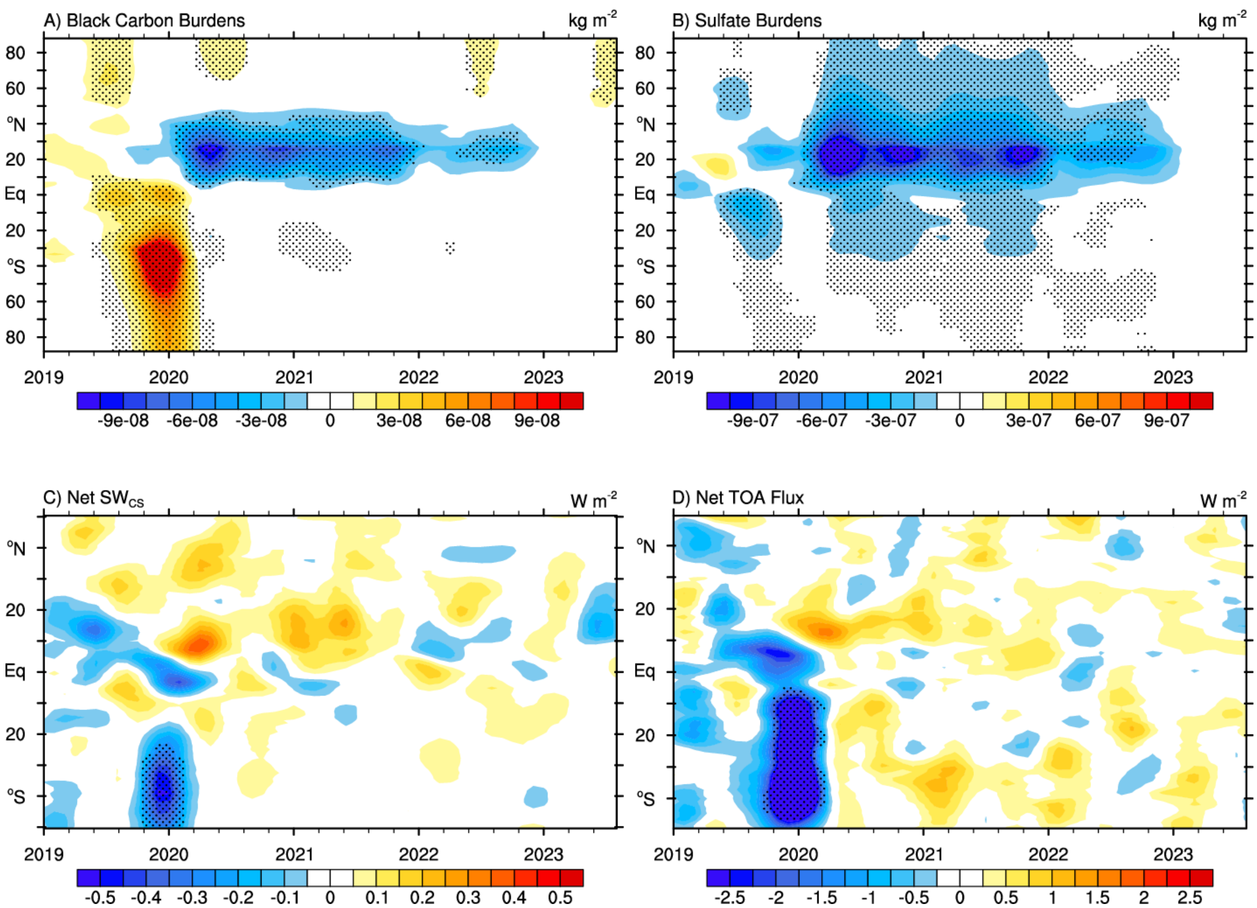

Figure 2: Zonal- and ensemble-mean evolution of COVID+AF differences with GSSP245 in (**a**) black carbon and (**b**) sulfate aerosol burdens, and net top-of-atmosphere clear-sky shortwave (**c**)

and net radiative flux (**d**). Stippling indicates regions of where differences exceed twice the ensemble standard error and fields are plotted through 2023 to focus on detectible differences.

The temporal evolution of large-scale (global-mean) climate responses to COVID and AF emissions anomalies is shown in Figure 3. For AF, the global TOA net SW flux (SW_{NET}, Figure 3a) is characterized by a rapid and intense reduction that peaks at −0.95 W m^{-2} in November 2019, with a two standard error range (2SE) of 0.15 W m^{-2}. The reduction is not long-lived however and by mid-2020 anomalies are negligible. In contrast, SW_{NET} anomalies due to COVID are small but persistent, peaking at 0.22±0.12 W m^{-2} in late 2020 and declining gradually through the integration period, with negative anomalies in the ensemble mean emerging in early 2023. Compensation of SW_{NET} anomalies by longwave anomalies is generally negligible, and TOA R_T (Figure 3b) anomalies therefore largely resemble those of SW_{NET} for both AF and COVID. A notable exception is the 2021-2023 COVID response, where the Planck response to surface warming is consistent with a reduction in R_T anomalies over time as climate warming enhances radiation to space. As a result, the 2SE range in R_T encompasses zero in early 2021. The evolution of global 2-meter air temperature anomalies (T_S, Figure 3c) depicts a rapid cooling in response to AF, reaching a minimum in late 2020 of −0.06 K, though with substantial uncertainty as the 2SE range is 0.04 K. Nevertheless, the cooling response is notable given the compensating effects of rapid cloud adjustments identified as commonly associated with biomass emissions (Stjern et al., 2017). The magnitude of peak warming arising from COVID (0.05 K) is almost as large as the AF cooling and also has considerable uncertainty (0.04 K). Responses in global precipitation (P) of approximately 0.2% are also small but detectible in both ensembles. Specifically, in AF, there is a reduction in 2020 and 2021 that peaks at −0.008±0.004 mm day^{-1}

in mid-2020; and there is an increase in COVID that peaks at 0.006±0.004 mm day^{-1} in mid-2021.

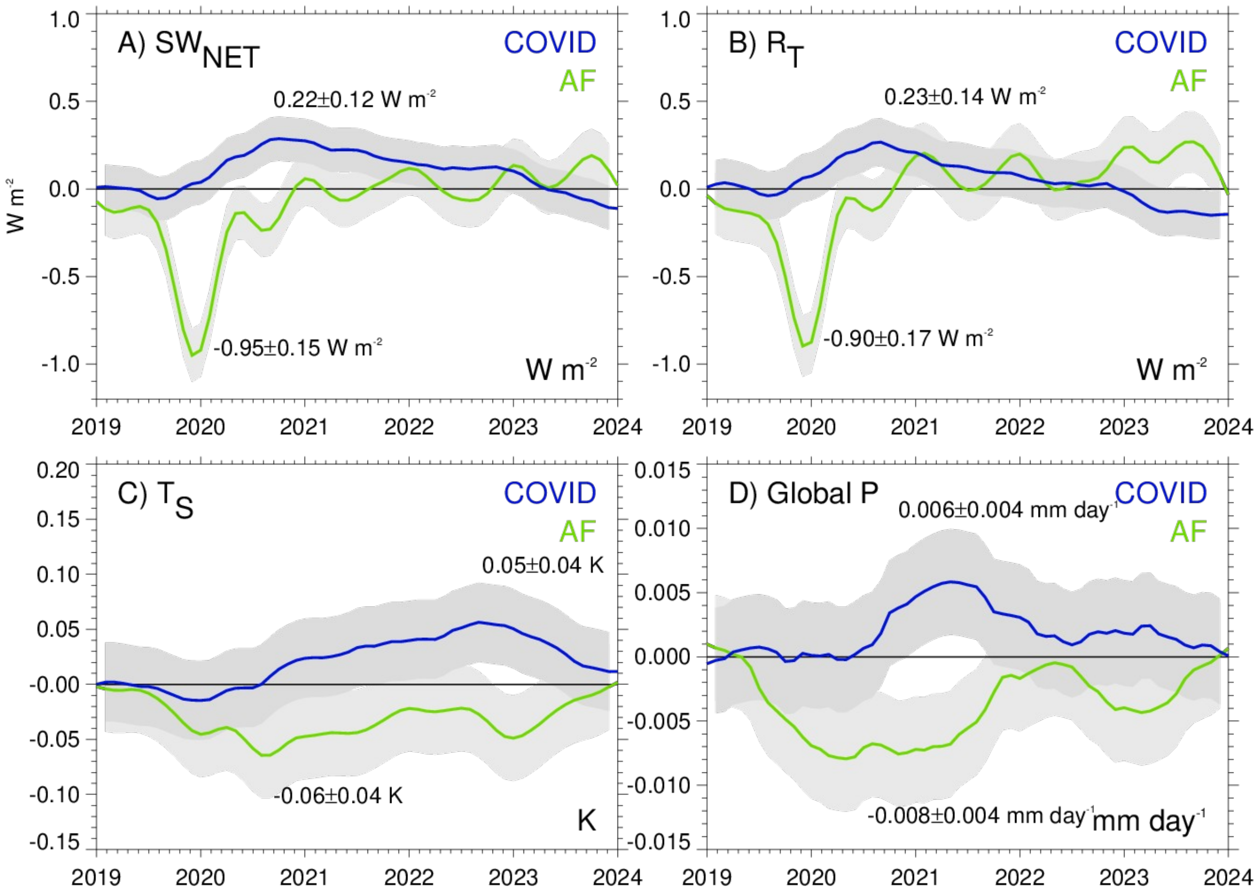

Figure 3: Evolution of a few key global-mean climate responses to AF and COVID emissions anomalies: (**a**) TOA SW_{NET} flux, (**b**) TOA R_T flux, (**c**) surface temperature, and (**d**) precipitation. Shaded regions and uncertainty ranges denote twice the ensemble standard error ranges and indicated values denote response extrema.

The spatial structures of peak climate responses in a few key fields are shown in Figure 4. Positive BC anomalies in AF (Figure 4a) span almost the entirety of the SH in December 2019 with the greatest anomalies coincident with, and downwind from, fires in Southeastern Australia. Notably, a secondary maximum also exists in the tropical Atlantic and African regions, likely due to regional deep convection and associated tropospheric convergence. In contrast, the largest negative BC anomalies due to COVID (Figure 4b) reside in the Northern Hemisphere, and particularly in Southeast Asia. Other detectable BC anomalies are present in each hemisphere though magnitudes are generally small relative to those for AF. The SW_{CS} flux response to AF (Figure 4c) is characterized by considerably greater spatial variability than for BC burdens, with reductions across much of the Southern Ocean and increases in regions where aerosol albedo differences with the surface are negative, with BC aerosols being particularly absorptive and therefore less reflective than bright surfaces, such as sea ice, Antarctica, and Australia's arid regions. Positive regional anomalies are also evident in the Northern Hemisphere Inter-Tropical Convergence Zone (ITCZ) and are likely due to enhanced convergence of water vapor (which increases SW_{CS} through absorption) due to a collocated strengthening of the ITCZ (discussed below). Responses in SW_{CS} to COVID (Figure 4d) are spatially complex but characterized mainly by positive anomalies in regions of peak emissions reductions in Southeast Asia. Due to the influence of internal variability, few detectible positive SW_{CS} anomalies are coincident with aerosol reductions in other regions. Significant negative anomalies in precipitable water (PW, Figure 4e) span the equatorial regions and southern tropics in response to AF, while positive anomalies span much of the northern tropics and subtropics – anomalies that together reflect a northward displacement of the ITCZ. Examining associated precipitation anomalies (Figure 4f) shows a noisier and more equatorially confined pattern of anomalies, but nonetheless one that is consistent with a northward ITCZ displacement.

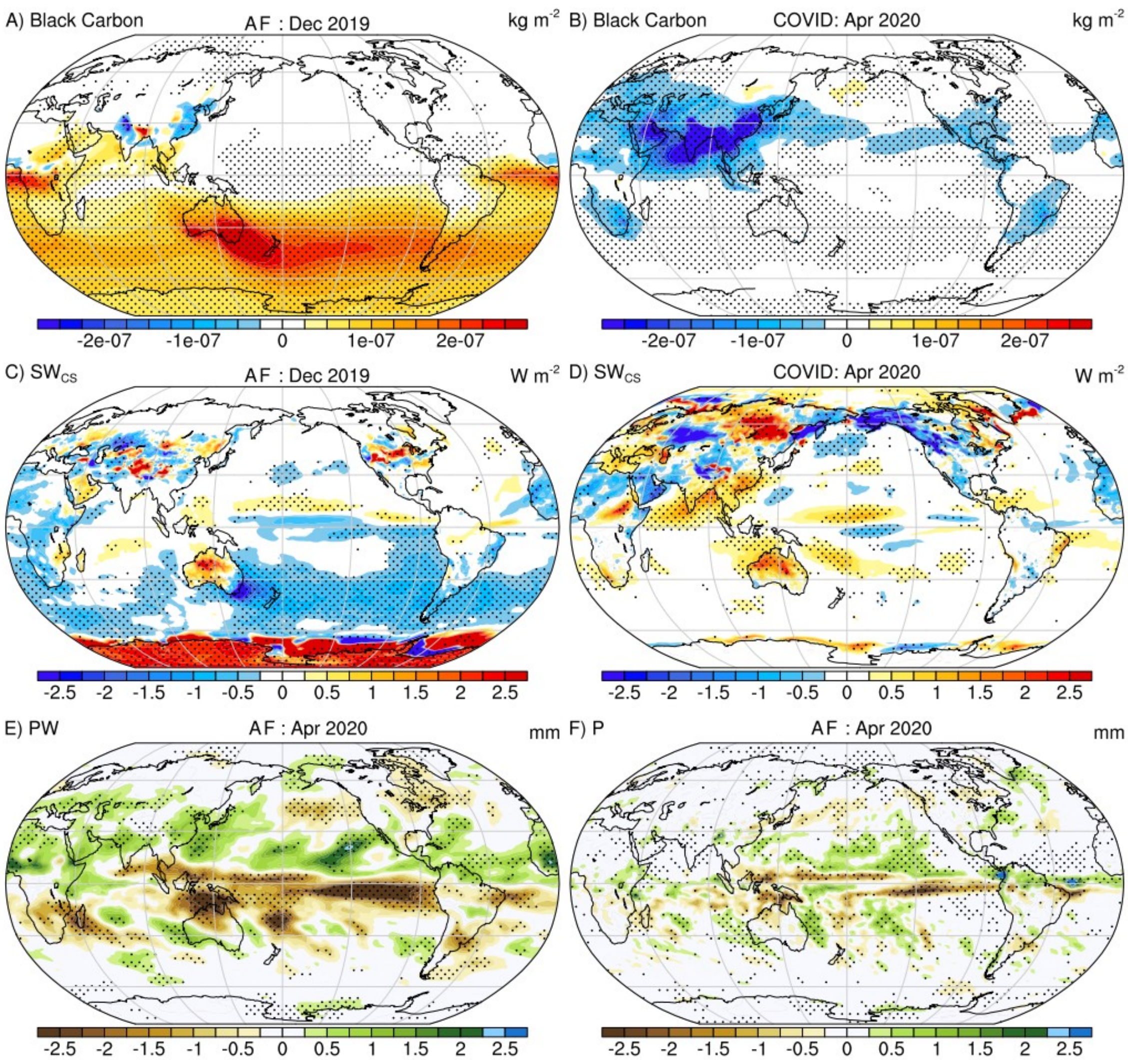

Figure 4: Spatial structure of key AF (**a**, **c**, **e**, **f**) and COVID (**b**, **d**) climate responses including black carbon burdens (**a, b**), and net clear-sky shortwave flux (**c, d**). Also shown are indicators of ITCZ displacement for AF including precipitable water € and precipitation (**f**). A seasonal gaussian smoother has been applied to all fields including COVID responses. Regions where the

ensemble mean exceeds twice the standard error are stippled. The fields represent means for the indicated months.

4 Conclusions

Using 50-member ensembles that provide insight not available in observations alone, our results highlight the intrinsic characteristics, similarities, and contrasts in the coupled climate responses to the AF and COVID events. These ensembles also allow for the projection of associated climate responses over the coming years. While both events perturb the TOA radiative imbalance, with detectible impacts on hemispheric energy budgets and surface temperature, the intensity and timescales of both the forcings and responses are found to differ considerably. The effects of COVID are generally subtle and gradual, and on a large scale are a challenge to distinguish from internal variability, as also discussed in Ming et al. (2020) and Loeb et al. (2021). In contrast, as shown in this and other recent works (Khaykin et al., 2020, Hirsch and Koren, 2021), the AF emissions anomalies are relatively brief but intense, and associated climate responses in many respects resemble a major SH volcanic eruption. The similarity includes for example an amplification of radiative effects via clouds, an associated rapid cooling of the SH, and a northward displacement of the ITCZ.

A range of caveats apply to our model simulations. Uncertainty in the forcing datasets is considerable and these include estimates of COVID-related emissions reductions and associated multi-year projections of depressed economic activity. These concerns are heightened by recent work that finds regional aerosol optical depth anomalies to be undetectable in March 2020 (Ming et al., 2020; Loeb et al., 2021). While AF emissions anomalies drive a stronger overall net radiative forcing, and therefore provide a clearer signal relative to internal variability, various sources of uncertainty also exist including the prescribed emissions estimates (see Methods, Pan et al. 2020). Lastly, there is the issue of uncertainty in CESM2 and particularly its representations of cloud-aerosol interactions that are central to the AF climate response. This issue is heightened by the fact that perturbations in clear-sky fluxes are nearly an order of magnitude smaller than in all-sky fluxes (Figures 2, S1). In addition, fluxes equatorward of the emissions are a key contributor to the overall hemispheric and planetary energy budget responses. It is therefore imperative that both simulated aerosol-cloud interactions and meridional and vertical redistribution of associated burdens and cloud properties be evaluated to bolster confidence in our experiments.

A final fundamental issue is the extent to which model responses to AF and COVID are consistent with observations. For example, it remains an open question whether the record warm temperatures reported in 2020 (e.g., Cheng et al. 2021) occurred despite the AF and COVID events or because of them? Our experiments suggest the net contribution was one of a slight cooling but as discussed above, important uncertainties exist. In CERES data, Loeb et al. (2021) identify the AF as being associated with a record maximum in SH aerosol optical depth, with a strong interhemispheric contrast. In our simulations, AF also drive a SH aerosol optical depth maximum and a substantial associated interhemispheric R_T gradient anomaly (1.68 ± 0.24 W m^{-2}, Figure S2). CERES data depict an anomalous R_T gradient (1.1 W m^{-2}) that is well within the ensemble spread of our simulations, and both these estimates and our simulations are consistent with the estimated AF reduction in downwelling surface SW radiation of 3 Wm^{-2} from 25^o-60^oS in Khaykin et al., 2020. A direct comparison to nature in these aspects is unfortunately complicated by the fact that our simulations don’t incorporate individual fires after 2018 except for the Australian wildfire outbreak from July 2019 through June 2020. There are also major caveats involved in comparing ensemble averages to a single realization in nature. Nonetheless, as shown here and anticipated from prior work (e.g., Fasullo et al, 2019; Pausata et al., 2020), a gradient of this magnitude would be anticipated to drive strong regional responses, both in the water cycle and in internal modes of variability such as ENSO. Future work will explore these responses to more fully understand the influence of these recent exceptionally anomalous events on the Earth system.

Acknowledgments, Samples, and Data

This material is based upon work supported by the National Center for Atmospheric Research (NCAR), which is a major facility sponsored by the National Science Foundation (NSF) under Cooperative Agreement 1852977. The CESM project is supported primarily by the NSF. Computing and data storage resources, including the Cheyenne supercomputer (doi:10.5065/D6RX99HX), were provided by the Computational and Information Systems Laboratory (CISL) at NCAR. We thank all the scientists, software engineers, and administrators who contributed to the development of CESM2. JF was partially supported by NASA Award 80NSSC17K0565, NSF Award AGS-1419571, and the Regional and Global Model Analysis (RGMA) component of the Earth and Environmental System Modeling Program of the U.S. Department of Energy's Office of Biological and Environmental Research (BER) via National Science Foundation IA 1844590. We acknowledge the assistance of Louisa Emmons in the preparation of emissions datasets.

Author contributions

JF initiated this study, contributed to the experiment design, analyzed results, prepared the figures, and first manuscript. RB and LE prepared forcing datasets for the COVID and COVID+AF experiments. All authors contributed to experiment design, discussions, interpretation of results, and manuscript revisions. NR conducted the simulations.

Competing interests

The authors declare no competing interests.

Data and materials availability

The data supporting the conclusions of this paper can be found on the Earth System Grid Federation (https://www.earthsystemgrid.org). Simulation output is available on NCAR's Digital Asset Services Hub (DASH, dash.ucar.edu). CERES EBAF Ed4.1 data is available at https://ceres.larc.nasa.gov/data/ .

References

Bogenschutz, P. A., Gettelman, A., Morrison, H., Larson, V. E., Craig, C., & Schanen, D. P. (2013). Higher−order turbulence closure and its impact on climate simulation in the Community Atmosphere Model. *Journal of Climate*, *26*, 9655–9676.

Danabasoglu, G., Lamarque, J.-F., Bacmeister, J., Bailey, D. A., DuVivier, A. K., Edwards, J., et al. (2020). The Community Earth System Model version 2 (CESM2). *Journal of Advances in Modeling Earth Systems*, *12*(2), e2019MS001916.

Dowdy, A. J., Ye, H., Pepler, A., Thatcher, M., Osbrough, S. L., Evans, J. P., et al. (2019). Future changes in extreme weather and pyroconvection risk factors for Australian wildfires. *Scientific reports, 9*(1), 1–11.

Fasullo, J. T., Otto−Bliesner, B. L., & Stevenson, S. (2019). The influence of volcanic aerosol meridional structure on monsoon responses over the last millennium. *Geophysical Research Letters*, *46*(21), 12350–12359.

Fasullo, J. T. (2020). Evaluating simulated climate patterns from the CMIP archives using satellite and reanalysis datasets using the Climate Model Assessment Tool (CMATv1). *Geoscientific Model Development*, *13*(8), 3627–3642.

Forster, P. M., Forster, H. I., Evans, M. J., Gidden, M. J., Jones, C. D., Keller, C. A., et al. (2020). Current and future global climate impacts resulting from COVID-19. *Nature Climate Change, 10*, 913–919.

Gettelman, A., & Morrison, H. (2015). Advanced two−moment bulk microphysics for global models. Part I: Off−line tests and comparison with other schemes. *Journal of Climate, 28*, 1268–1287.

Gettelman, A., Lamboll, R., Bardeen, C. G., Forster, P. M., & Watson−Parris, D. (2020). Climate Impacts of COVID−19 Induced Emission Changes. *Geophysical Research Letters*, e2020GL091805.

Giglio, L., Randerson, J. T., & van der Werf, G. R. (2013). Analysis of daily, monthly, and annual burned area using the fourth−generation global fire emissions database (GFED4) *Journal of Geophysical Research Biogeosciences*, *118*, 317–328.

Hirsch, E., & Koren, I. (2021). Record-breaking aerosol levels explained by smoke injection into the stratosphere. *Science*, *371*, 6535, 1269–1274.

Hoose, C., Kristjánsson, J. E., Chen, J.−P., & Hazra, A. (2010). A classical−theory−based parameterization of heterogeneous ice nucleation by mineral dust, soot, and biological particles in a global climate model. *Journal of the Atmospheric Sciences, 67*, 2483–2503.

Khaykin, S., Legras, B., Bucci, S., Sellitto, P., Isaksen, L., Tence, F., et al. (2020). The 2019/20 Australian wildfires generated a persistent smoke-charged vortex rising up to 35 km altitude. *Communications Earth and Environment*, *1*(22), 1–12.

Lamboll, R. D., Jones, C. D., Skeie, R. B., Fiedler, S., Samset, B. H., Gillett, N. P., et al. (2020a). Modifying emission scenario projections to account for the effects of COVID-19: Protocol for Covid-MIP. *Geoscientific Model Development Discussions*, 1-20.

Lamboll, R., Forster, P., & Rogelj, J. (2020b). Emissions changes in 2020 due to Covid19 (Version 4.0) [Data set]. Zenodo. http://doi.org/10.5281/zenodo.3947917.

Le Quéré, C., Jackson, R. B., Jones, M. W., Smith, A., Abernethy, S., Andrew, R., et al. (2020). Temporary reduction in daily global CO2 emissions during the COVID-19 forced confinement. *Nature Climate Change*, *10*, 647–653.

Liu, X., Ma, P. L., Wang, H., Tilmes, S., Singh, B., Easter, R. C., et al. (2016). Description and evaluation of a new four−mode version of the Modal Aerosol Module (MAM4) within Version 5.3 of the Community Atmosphere Model. *Geoscientific Model Development, 9*, 505–522.

Loeb, N. G., Su, W., Bellouin, N., & Ming, Y. (2021). Changes in clear−sky shortwave aerosol direct radiative effects since 2002. *Journal of Geophysical Research: Atmospheres*, e2020JD034090.

Ming, Y., Lin, P., Naik, V., Paulot, F., Horowitz, L. W., Ginoux, P. A., et al. (2021). Assessing the influence of COVID−19 on the shortwave radiative fluxes over the East Asian marginal seas. *Geophysical Research Letters, 48*(3), e2020GL091699.

Pan, X., Ichoku, C., Chin, M., Bian, H., Darmenov, A., Colarco, P., Ellison, L., Kucsera, T., da Silva, A., Wang, J., Oda, T., and Cui, G.: Six global biomass burning emission datasets: intercomparison and application in one global aerosol model, Atmos. Chem. Phys., 20, 969–994, 2020.

Pausata, F. S., Zanchettin, D., Karamperidou, C., Caballero, R., & Battisti, D. S. (2020). ITCZ shift and extratropical teleconnections drive ENSO response to volcanic eruptions. *Science Advances, 6*(23), eaaz5006.

Randerson, J. T., Chen, Y., van der Werf, G. R., Rogers, B. M., & Morton, D. C. (2012), Global burned area and biomass burning emissions from small fires. *Journal of Geophysical Research, 117*, G04012.

Sharples, J. J., Cary, G. J., Fox-Hughes, P., Mooney, S., Evans, J. P., Fletcher, M.-S., et al. (2016). Natural hazards in Australia: Extreme bushfire. *Climatic Change, 139*, 85–99.

Shi, X., Liu, X., & Zhang, K. (2015). Effects of preexisting ice crystals on cirrus clouds and comparison between different ice nucleation parameterizations with the Community Atmosphere Model (CAM5). *Atmospheric Chemistry and Physics, 15*, 1503–1520.

Sokolik, I. N., Soja, A. J., DeMott, P. J., & Winker, D. (2019). Progress and challenges in quantifying wildfire smoke emissions, their properties, transport, and atmospheric impacts. *Journal of Geophysical Research: Atmospheres*, *124*, 13,005–13,025.

Stjern, C. W., Samset, B. H., Myhre, G., Forster, P. M., Hodnebrog, Ø., Andrews, T., et al. (2017). Rapid adjustments cause weak surface temperature response to increased black carbon concentrations. *Journal of Geophysical Research: Atmospheres, 122*, 11,462–11,481.

Tilmes, S., Hodzic, A., Emmons, L. K., Mills, M. J., Gettelman, A., Kinnison, D. E., et al. (2019). Climate forcing and trends of organic aerosols in the Community Earth System Model (CESM2). *Journal of Advances in Modeling Earth Systems, 11*, 4323–4351.

van der Werf, G. R., Randerson, J. T., Giglio, L., van Leeuwen, T. T., Chen, Y., Rogers, B. M., et al. (2017). Global fire emissions estimates during 1997–2016. *Earth System Science Data, 9*, 697–720.

van Marle, M. J. E., Kloster, S., Magi, B. I., Marlon, J. R., Daniau, A.-L., Field, R. D., et al. (2017). Historic global biomass burning emissions for CMIP6 (BB4CMIP) based on merging satellite observations with proxies and fire models (1750–2015). *Geoscientific Model Development, 10*, 3329–3357.

Wang, Y., Liu, X., Hoose, C., & Wang, B. (2014). Different contact angle distributions for heterogeneous ice nucleation in the Community Atmospheric Model version 5. *Atmospheric Chemistry and Physics*, *14*, 10411–10430.

Wintle, B. A., Legge, S., & Woinarski, J. C. (2020). After the megafires: What next for Australian wildlife? *Trends in Ecology & Evolution, 35*(9), 753–757.

Supplementary Information

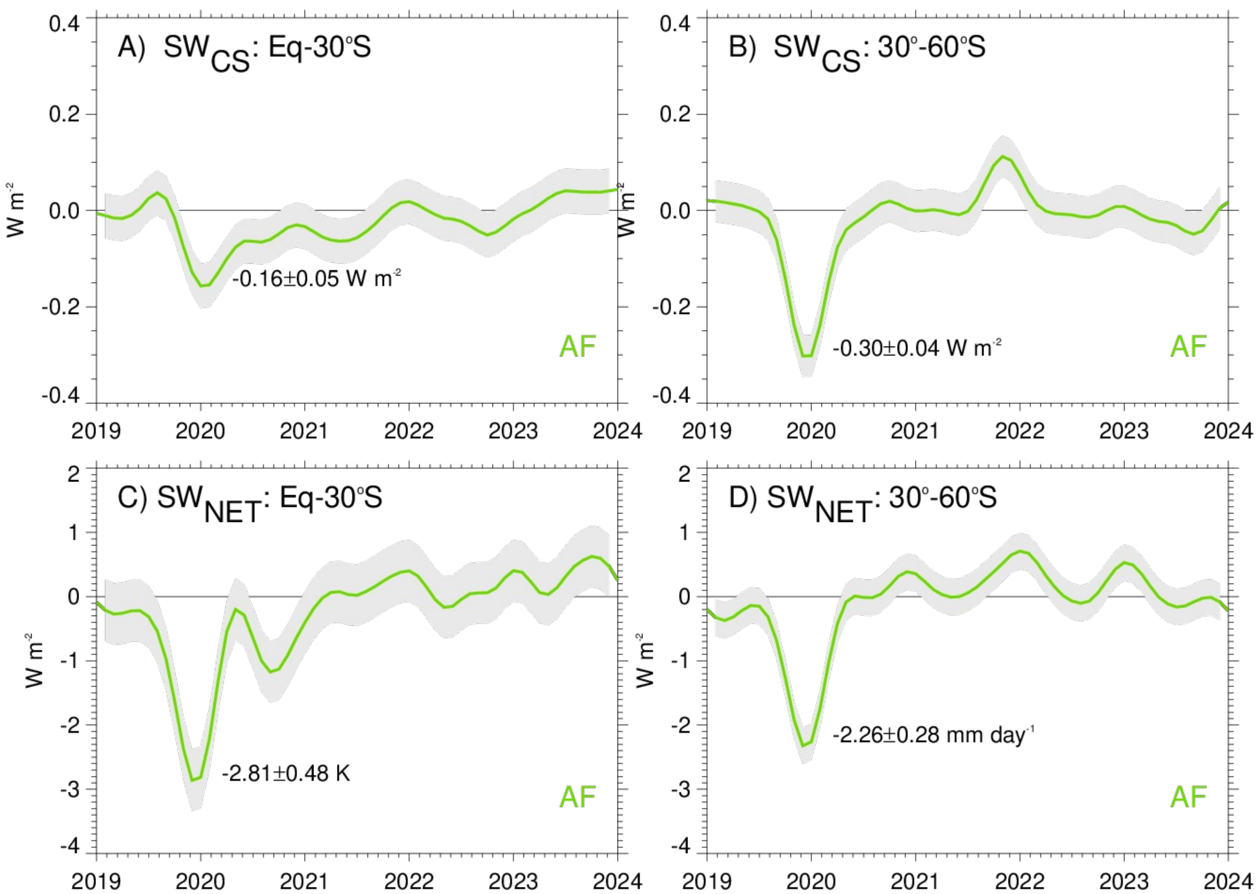

Figure S1: Responses of key TOA SW fluxes over ocean to AF emissions anomalies, including SW_{CS} from (a) the Equator to 30°S and (b) 30°-60°S; and SW_{NET} from (c) the Equator to 30°S and (d) 30°-60°S (d). Shaded regions denote twice the ensemble standard error ranges and plotted values denote response magnitudes in January 2020. Indicated values denote response extrema.

461

462

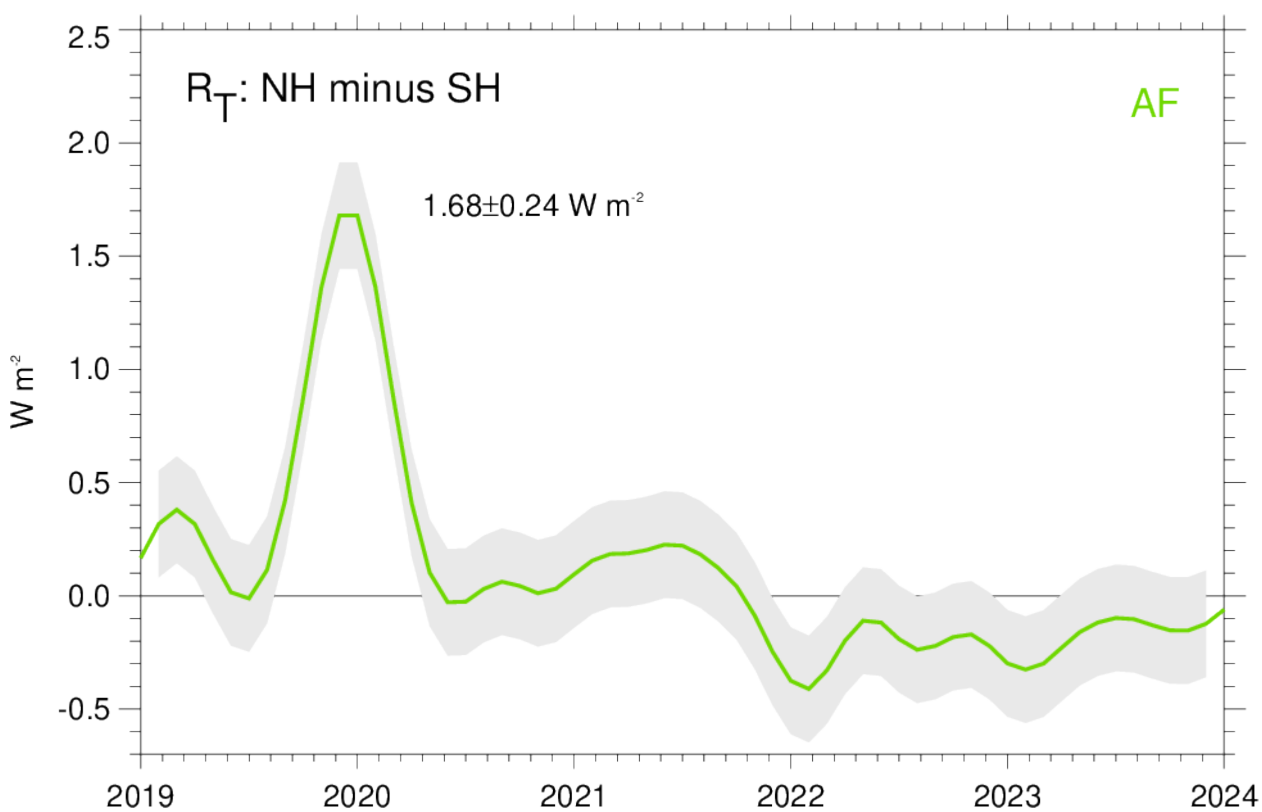

R_T: NH minus SH
AF
1.68±0.24 W m-2
W m-2
2.5
2.0
1.5
1.0
0.5
0.0
-0.5
2019
2020
2021
2022
2023
2024

Figure S2: Response in contrast in TOA radiative imbalance between Northern and Southern Hemisphere due to AF. Indicated value denotes response extrema. Shading indicates two times the ensemble standard error.